Thermographic Network Identification for Non-Destructive Testing

by Simon H. Anke[*], Nils J. Ziegeler[*], Peter W. Nolte[**], Stefan Schweizer[*,**]

*   *South Westphalia University of Applied Sciences, Faculty of Electrical Engineering, Soest, Germany*
**   *Fraunhofer Application Center for Inorganic Phosphors, Branch Lab of Fraunhofer Institute for Microstructure of Materials and Systems IMWS, Soest, Germany*

Abstract

The method of thermographic network identification is investigated for its performance in defect detection using a flat-bottom holes test sample. Thermographic measurements based on pulsed and step excitation are evaluated using thermographic network identification and thermographic signal reconstruction. To determine the performance of the methods, a sensitivity index is used as a measure of defect visibility. The comparison shows that thermographic network identification is a competitive method for defect detection with potential for further optimization.

1. Introduction

Thermography is a well-established technique for non-destructive testing. In general, thermographic techniques can be divided into two subgroups, namely active and passive thermography. While passive thermography observes the infrared radiation emitted from an object on its own, in active thermography, the sample is heated with pre-determined patterns. Many different heat sources, excitation modes, and evaluation algorithms are available which can be combined to create a wide range of thermographic techniques [1]. Typical heat sources include halogen lamps, resistive heating, eddy-currents, and lasers. Suitable combinations of excitation source and algorithm allow for defect recognition and classification in many application fields as well as the measurement of material parameters such as layer thickness or thermal resistances.

Each evaluation technique available in thermographic non-destructive testing is based on a unique approach to visualize and interpret the thermographic data. The method of principal component thermography, for example, looks at the data from a statistical point of view. The thermal transient of a pulse-heated specimen is decomposed by singular value decomposition using empirical orthogonal functions. These functions classify the characteristic variability of the data, separating noise from signal [2]. Another example for an evaluation technique based on pulse-heating excitation is pulsed phase thermography. In this method, the Fourier components of the signal form a basis for the analysis. From its real and imaginary parts, the signal phase is calculated for each pixel of the thermographic image and visualized, for example for defect detection [3]. A common evaluation technique remaining purely in the time-domain is thermographic signal reconstruction (TSR). There, a double-logarithmic polynomial is approximated to the thermal transient. For defect detection, either the evaluation of the resulting polynomial coefficients or the polynomial itself and its derivative are suitable [4].

The recently introduced method of thermographic network identification (TNI) [5] uses a different approach for the analysis. It calculates a thermal equivalence network for each pixel in the thermographic sequence and analyses the network parameters for defect detection. In TNI, the transient response of a device under test to a step in the heating power is evaluated. The main result of TNI is the time constant spectrum. It is calculated for each pixel in the thermographic sequence. The resulting spectra are combined to form images for the same time constant. The amplitude of a spectrum is converted to a specific colour in the corresponding colour map representation. Defects are analysed by their impact on this spectrum. In principle, using pulse heating for TNI is also possible. Ideally, the entire heating and cooling phase is recorded in this case.

The classification of visibility of image features is a typical problem in signal detection theory. A commonly used approach is to use a sensitivity index. In this work, it is applied to evaluate the thermographic images obtained from pulse and step excitation and the subsequent analysis. The sensitivity index is a dimensionless quantity to quantify the difference between two distributions. The result of each method is analysed to find out to what degree each flat-bottom hole of the test sample is visible. Expressed in decibel, the sensitivity index gives an objective measure of the detection performance for the different methods.

In this work, the performance of TNI and TSR in defect detection is evaluated using a flat-bottom-holes board as a test sample. The sample has 16 holes of different diameters and depths. Pulse and step heating measurements are performed on the sample and evaluated using a wide range of variants from TNI and TSR. The used thermographic algorithms and the evaluation methodologies are presented in detail. To guarantee an objective evaluation, the signal-to-noise ratio of each defect is calculated based on the relative signal strength and variance. Using these results, the specific experimental challenges and opportunities of TNI are discussed.

2. Theory

2.1 Thermographic signal reconstruction

Thermographic signal reconstruction [6] is a commonly used and widely accepted evaluation technique, known for its effectiveness and simplicity. It provides a significant improvement in the signal-to-noise ratio compared to the measured raw data and is thus able to detect small and deep defects. Both pulse-heated and step-heated measurement series can be analysed [4, 7]. In principle, both excitation variants can also be evaluated with TNI. This makes TSR an attractive method for comparison with TNI. Typically, pulse excitation is used for TSR as it provides better results than step excitation [7].

In the following, a brief introduction to the main equations of TSR is given. The model underling TSR is a semi-infinite homogeneous body, which is excited by an idealized Dirac pulse. The resulting thermal transient is analysed,

$$T(t) = T_0 + \frac{Q}{e\sqrt{\pi t}} \,, \tag{1}$$

where T_0 is the initial temperature, Q the energy density, and e the thermal effusivity. Converting and transforming (1) into a logarithmic form, $z = \ln(t)$, yields

$$\ln(T(t) - T_0) = \ln(\Delta T(t)) = \ln\left(\frac{Q}{e\sqrt{\pi}}\right) - \frac{1}{2}\ln(t) = \text{const.} - \frac{1}{2} \cdot z \,. \tag{2}$$

In a double-logarithmic plot, this results in a slope of $-1/2$ for areas without defects. For short and long times, the thermal transients observed over defective areas is equal to defect-free areas. For the time in between, the behaviour varies due to thermal obstacles, which forms the basis for a TSR analysis. For the evaluation, the thermal transient is approximated by a double logarithmic polynomial, i.e.,

$$\ln(\Delta T(z)) \approx \sum_{i=0}^{N} a_i z^i = T_{\text{TSR}}(z) \,. \tag{3}$$

For a defect-free area, a second-degree polynomial is sufficient for the approximation, as in this case the thermal transient is almost linear. To map defects as well, polynomials of degree 4 to 11 are usually used [8]. For step excitation, the characteristic slope is $+1/2$ at the beginning and increases to $+1$ in the further course. For details regarding TSR using step excitation, the reader is referred to [4, 7].

2.2 Thermographic network identification

In thermographic network identification, the step response is characterized by the thermal impedance, Z_{th}, in logarithmic time, $z = \ln(t)$. To obtain the step response, the specimen is heated to thermal equilibrium at an elevated temperature. Then, the heat source is turned off. The thermal impedance is calculated from the measured transient, $T(t)$, and the initial temperature, T_0, via

$$Z_{\text{th}}(t) = \frac{T_0 - T(t)}{P} \quad \text{and} \quad a(z) = Z_{\text{th}}(t = \exp(z)) \,. \tag{4}$$

If the heating power, P, is known, the thermal resistances and capacities of the sample are obtained exactly, given a suitably one-dimensional heat path. For the evaluation in this work, P is set to unity as this does not affect defect detection. In a first step of the evaluation, the step response, i.e. the thermal impedance in logarithmic time, $a(z)$, is differentiated to obtain the impulse response, $\partial_z a(z) = h(z)$.

The quantity used for defect detection is the time constant spectrum, $R(\zeta)$. It represents the different times scales at which the temperature relaxation occurs. Thus, it is related to the thermal resistances and capacities of the subsurface structure, i.e. the defects. Computationally, the time constant spectrum is connected to $h(z)$ via a convolution equation,

$$h(z) = \int_{-\infty}^{\infty} R(\zeta) \exp(z - \zeta - \exp(z - \zeta))\mathrm{d}\zeta = (R \otimes w_z)(z) \,, \tag{5}$$

where $w_z(z) = \exp(z - \exp(z))$.

To extract the time constant spectrum from 5, Bayesian deconvolution is the most suitable method. This method is based on Bayes' theorem, a computational tool to quantify beliefs based on evidence. Here, the evidence is the impulse response, $h(z)$. The goal is to find the most likely guess for the time constant spectrum. Bayesian deconvolution achieves this by solving an iterative formula using $h(z)$ and $w_z(z)$. In the following, a brief description of the main iteration formula of Bayesian deconvolution is given [9]. The starting point is Bayes' theorem,

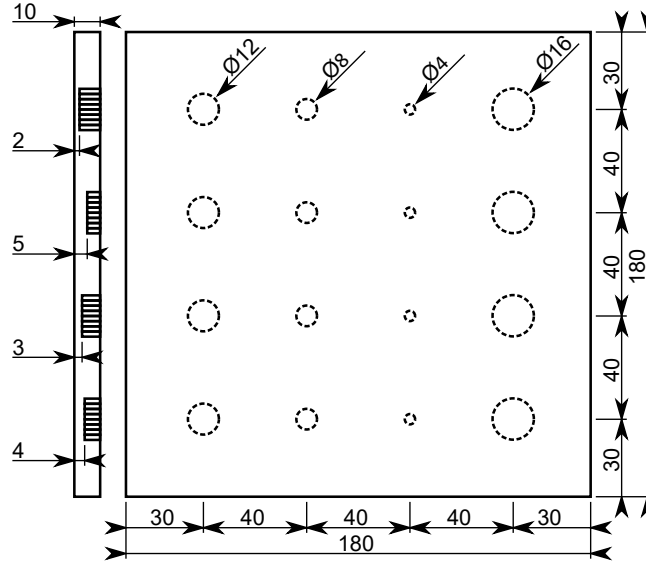$$P(R|h) = \frac{P(h|R)P(R)}{P(h)} \,. \tag{6}$$

Fig. 1. *Schematic of the steel flat-bottom-holes sample, which was modelled on the test specimen from [10]. All sizes are stated in millimeter. Defects are labelled according to the notation: diameter/depth, e.g., 16/2 denotes the top right hole.*

The expression $P(R|h)$ describes the probability that a hypothesis, R, is valid given that the evidence, h, is true. This probability is related to the probability, $P(h|R)$, via the prior probabilities of R and h, $P(R)$ and $P(h)$. In the present case, the time constant spectrum, $R(\zeta)$, and the impulse response, $h(z)$, are vectors. Therefore, the theorem is reformulated in vector notation,

$$P(R_i|h_k) = \frac{P(h_k|R_i)P(R_i)}{\sum_j P(h_k|R_j)P(R_j)} \ . \tag{7}$$

Here, $P(R_i)$ is identified as R_i, i.e., the i-th component of the vector $R(\zeta)$. In a few steps, the iteration formula (8) results. $P(h_k|R_i)$ is identified as $w_z(z)$. In (8) it appears in matrix notation as W_{ki}, which can be obtained by writing the convolution (5) in matrix form. The more likely guess $R^{(n+1)}(z)$ is derived from its predecessor $R^{(n)}(z)$ via

$$R_i^{(n+1)} = R_i^{(n)} \sum_k \frac{h_k W_{ki}}{\sum_j W_{kj} R_j^{(n)}} \ . \tag{8}$$

The initial value $R^{(0)}(z)$ can be taken as $h(z)$, the end result should not depend on it. For thermographic network identification, a few hundred to a few thousand iteration steps are recommended to achieve a balance between speed and accuracy.

3. Experimental details

The flat-bottom-holes sample used in this work has the form of a 180 mm × 180 mm × 10 mm steel plate (Figure 1). The surface facing the camera is covered with black paint to enhance optical absorption as well as infrared emissivity. The sample features holes of varying depths (2 mm to 5 mm) and diameters (4 mm to 16 mm).

Measurements are performed using an InfraTec ImageIR 8380S thermography system (InSb detector). For pulse excitation, a Hensel EH Pro 6000 flash lamp is used. The sample is excited with a 6-kJ flash from a distance of approximately 70 cm. Due to the afterglow of the flash lamp, the first 20 ms after the pulse are discarded. For step heating, two different excitation sources are used. First, a 500-W halogen lamp is used for heating from a distance of approximately 40 cm. To reduce spectral overlap between the infrared detector and the halogen lamp, a PMMA filter is inserted between the specimen and the lamp [7]. In a second measurement series, an LED infrared excitation source is used [11]. As the center wavelength of the LED source is at 850 nm, there is no overlap with the thermography system. The specimen is excited from a distance of 40 cm with an optical power of 55 W. The step thermographic measurements are recorded at a sampling rate of 140 Hz. Then, the frequency is lowered to reduce the size of the measured data.
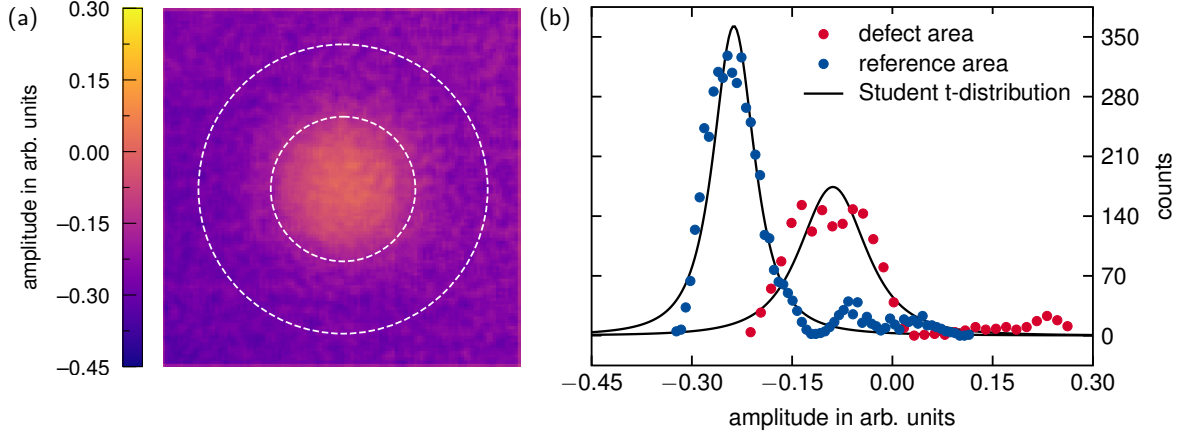
Fig. 2. *(a) Area selection for SNR calculation with the defect area in the inner circle and the reference area in the outer ring. (b) Fitted Student t-distribution. The defect investigated is 16/2 and the data used are the fitted polynomial coefficients a_1 for the pulse heated sample.*

4. Defect classification

To determine the defect visibility objectively, a quantifiable measure is needed. In the literature, the signal-to-noise ratio (SNR) is often used to classify whether a defect is visible [10, 12, 13]. An area containing the defect and a suitable reference region are chosen to calculate the SNR. Here, it is calculated as the logarithmic representation of the root-mean-square (RMS) sensitivity index, d'_a, via [14]

$$d'_a = \frac{1}{\sigma_{\text{RMS}}} |\overline{x}_{\text{defect}} - \overline{x}_{\text{reference}}| = \frac{\sqrt{2}}{\sqrt{\sigma_{\text{defect}}^2 + \sigma_{\text{reference}}^2}} |\overline{x}_{\text{defect}} - \overline{x}_{\text{reference}}| , \qquad (9)$$

where $\overline{x}$ and σ are the means and standard deviations of the analysed values in the corresponding areas. Typically, the signal-to-noise ratio is expressed in decibel [12], i.e.,

$$\text{SNR}_{\text{dB}} = 20 \cdot \log_{10}\left(d'_a\right) . \qquad (10)$$

Here, a defect is assumed to be identified unambiguously, if $|\overline{x}_{\text{defect}} - \overline{x}_{\text{reference}}| > 2\sigma_{\text{RMS}}$. Expressed in decibel, this leads to a SNR_{dB} of at least 6 dB. The visual contrast of a defect is determined relative to its immediate surrounding. As the defect regions are assumed to be known, each defect has its own reference region.

As an example, Figure 2(a) shows a defect with a diameter of 16 mm and a depth of 2 mm. The reference region has twice the diameter of the defect. The corresponding distributions of the individual areas are shown in Figure 2(b). As a calculation of mean value and standard deviation is quickly distorted by large outliers, a Student-t distribution is used here to minimize this effect. These outliers are caused, for example, by defective pixels in the detector and/or badly converging polynomial fits. The mean and standard deviation are determined from the model of the distribution. In case of Figure 2, they amount to $\overline{x}_{\text{defect}} = -0.0890$, $\overline{x}_{\text{reference}} = -0.2372$, $\sigma_{\text{defect}} = 0.0526$, and $\sigma_{\text{reference}} = 0.0336$. In this case, the defect has an SNR of

$$\text{SNR}_{\text{dB}} = 20 \cdot \log_{10}\left(\frac{\sqrt{2}}{\sqrt{0.0526^2 + 0.0336^2}} |(-0.0890) - (-0.2372)|\right) = 10.5272 \,\text{dB} . \qquad (11)$$

According to the above described 6-dB criterion, the defect is recognized, which matches well with the visual impression in Figure 2.
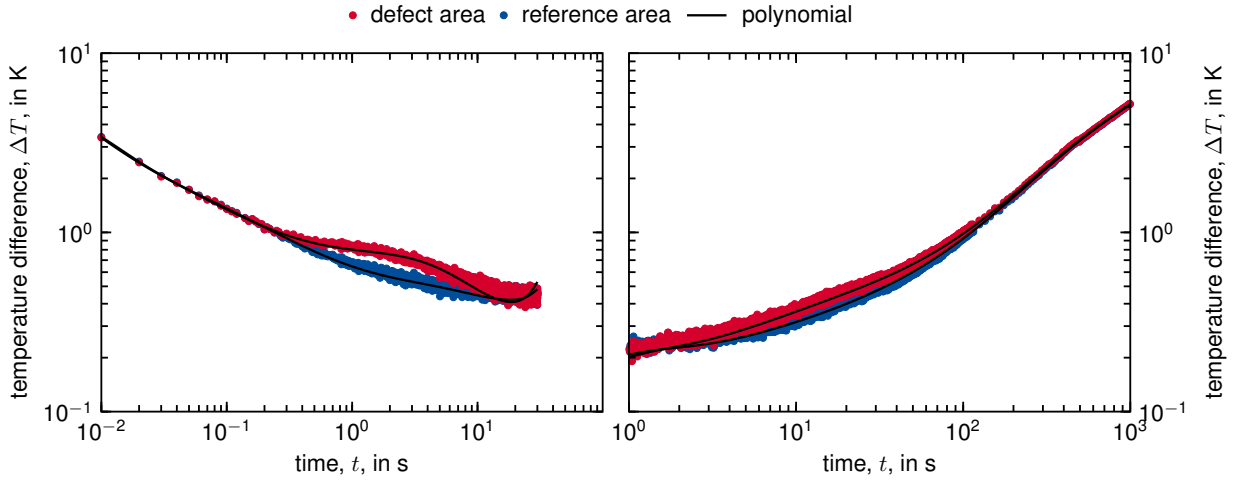
Fig. 3. *Average thermal transient of the reference and the defect area for defect 16/2 upon pulsed excitation (left) and LED step excitation (right). For the fits, polynomials of 7th degree are calculated for each pixel of the area. The figure shows the average values.*

5. Evaluation

5.1 Thermographic signal reconstruction

For thermographic signal reconstruction, polynomials of 4th to 11th degree are tested. In the following evaluation, a polynomial of 7th degree is chosen, as it provides the best results in terms of signal-to-noise ratio. As reference, the unaltered thermal transient for each measurement is also evaluated according to the procedure described above. In Figure 3, the measured thermal transients for defect 16/2 and the approximations by 7th-degree polynomials are shown for pulsed excitation (left) and for step excitation with a LED lamp (right). A clear separation between the average thermal transients in the defect and reference areas is visible. This difference is even more pronounced for pulse heating. Step excitation with a halogen lamp results in a similar behaviour. A difference, however, is observed in the total temperature difference, which amounts for the halogen lamp 18 K, while it is 14 K for the LED lamp.

As the data points are not evenly spaced in logarithmic time, an additional weighting is applied according to the local data density. This is challenging for thermographic measurements based on step excitation, as sparse sampling for short times leads to a relatively high impact of measurement noise. While this affects both TSR and TNI, polynomial least-squares fitting is in particular sensitive to outliers. Furthermore, polynomials have a difficulty mapping threshold effects [15]. To alleviate this effect, flat portions of pulse and step-heated thermal signals are truncated (Figure 3).

For non-destructive testing, usually the resulting polynomial coefficients, a_i, the approximated thermal signal, $\exp(T_{\text{TSR}})$, as well as the 1st and 2nd derivatives, $\partial_z T_{\text{TSR}}$ and $\partial_z^2 T_{\text{TSR}}$, are viewed [7, 8, 10] and serve as signal, x, in (9). The derivatives are calculated as

$$\frac{\text{d}}{\text{d}z} T_{\text{TSR}}(z) = \sum_{i=1}^{N} i a_i z^{i-1} \quad \text{and} \quad \frac{\text{d}^2}{\text{d}z^2} T_{\text{TSR}}(z) = \sum_{i=2}^{N} i(i-1) a_i z^{i-2} \, . \tag{12}$$

A moving average filter (3×3) is applied to all images. For defect classification, it is necessary to determine the mean and standard deviation of each defect and reference area. For all TSR results (polynomial coefficients, thermal transients, and derivatives) a Student-t distribution is fitted to the distributions. This distribution is more robust against outliers and is able to model non-Gaussian phenomena.

Depending on the variant of TSR evaluation, a large number of images has to be evaluated. For example, in the time sequence measurements ($T_{\text{TSR}}, \partial_z T_{\text{TSR}}$), each time frame is evaluated for each of the polynomial degrees. Thus, an automated evaluation is required and the procedure has to be robust. Challenges are posed by, for example, defective pixels of the detector and badly converging polynomial fits. In addition, statistical fluctuations in the images are significant, i.e., due to the high number of evaluations, sometimes defects are identified as false positive. Safeguards are implemented to double-check the validity of a detection.
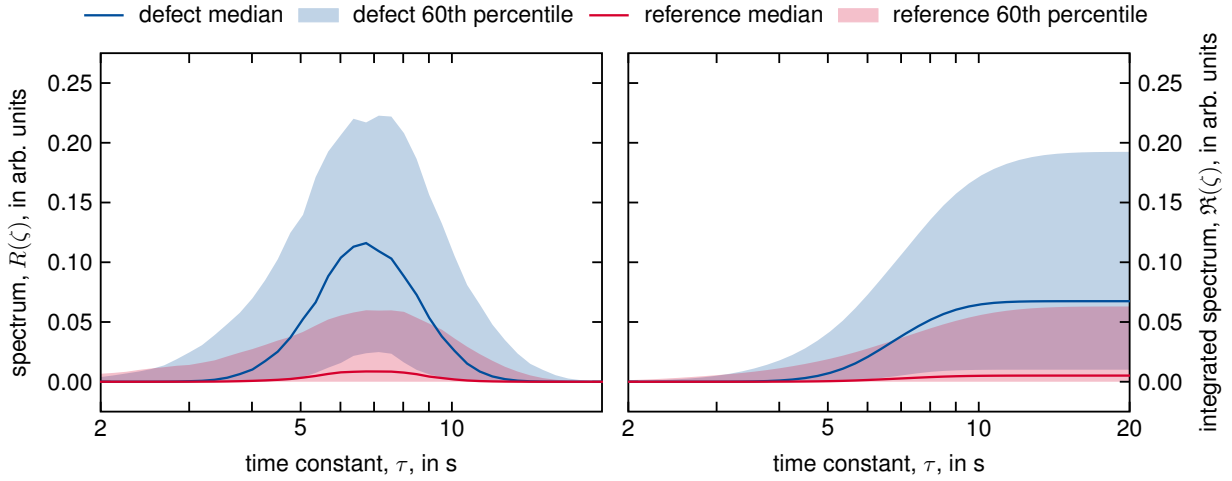
Fig. 4. *Median and interval between 20 % and 80 % of the cumulative distribution function for (left) the time constant spectrum, $R(\zeta)$, and (right) the integrated time constant spectrum, $\mathfrak{R}(\zeta)$, for the reference and defect area of defect 16/2.*

5.2 Thermographic network identification

Thermographic network identification is based on the equations given in Subsection 2.2. For details regarding the algorithm, the reader is referred to [5]. The resulting time constant spectra are evenly distributed in logarithmic time and are evaluated in the range between 1.5 s and 500 s. Smaller time constants are truncated, as the spectra show mainly noise there. For τ greater than 500 s, no defects are visible.

For defect detection, the time constant spectrum is calculated for each pixel of the thermographic transient. The amplitude of the time constant spectrum, R, serves as signal, x, in (9). Images are analysed for each value of τ, similar to the analysis by TSR. In addition, the integrated time constant spectrum, $\mathfrak{R}(\zeta)$, is calculated via

$$\mathfrak{R}(\zeta) = \int_{-\infty}^{\zeta} R(\zeta) \mathrm{d}\zeta\,. \tag{13}$$

A moving average filter is applied to all images. Figure 4 shows (left) the time constant spectrum, $R(\zeta)$, and (right) the integrated time constant spectrum, $\mathfrak{R}(\zeta)$, for defect 16/2. For defect classification in all TNI results, the mean values, $\overline{x}$, and standard deviations, σ, are determined using

$$\overline{x} = \frac{1}{N} \sum_{i=1}^{N} x_i \qquad \text{and} \qquad \sigma = \sqrt{\frac{1}{N} \sum_{i=1}^{N} (x - \overline{x})^2}\,. \tag{14}$$

This methodology is chosen, as the amplitude distributions of the time constant spectrum and the integrated time constant spectrum have significantly fewer outliers and do not, in general, follow a simple distribution.

5.3 Results

All evaluation methods provide a huge number of images as result, which have to be analysed to determine the best SNR for each defect. The SNR is calculated for each image independently, as described in Section 5. Note, that this automatic evaluation is not perfect. In come cases, a human observer might disagree on the visibility of a defect. It might happen that the maximum SNR is provided by a false positive detection, or, due to fluctuations, the maximum signal-to-noise ratio is overestimated. Therefore, a moving average is applied to the sequence of SNR results. Figure 5 shows exemplarily some visual impressions related to the different SNR. Table 1 collects the best SNR obtained for the various methods. The results are colour-coded to guide the eye. Defects with an SNR smaller than 0 dB are considered to be not detected and coloured in red. In this case, the mean values differ from each other less than the mean standard deviation, σ_{RMS}. Defects with an SNR above 6 dB are considered to be detected and coloured in green.

When comparing the measured thermal transient, ΔT, for flash, halogen, and LED excitation, the defects are easier to detect using flash excitation. This becomes obvious by comparing the SNR_{dB} for the most noticeable defect 16/2 and reflects a property of the experimental setup and the measurement method. However, the focus of this paper is to compare
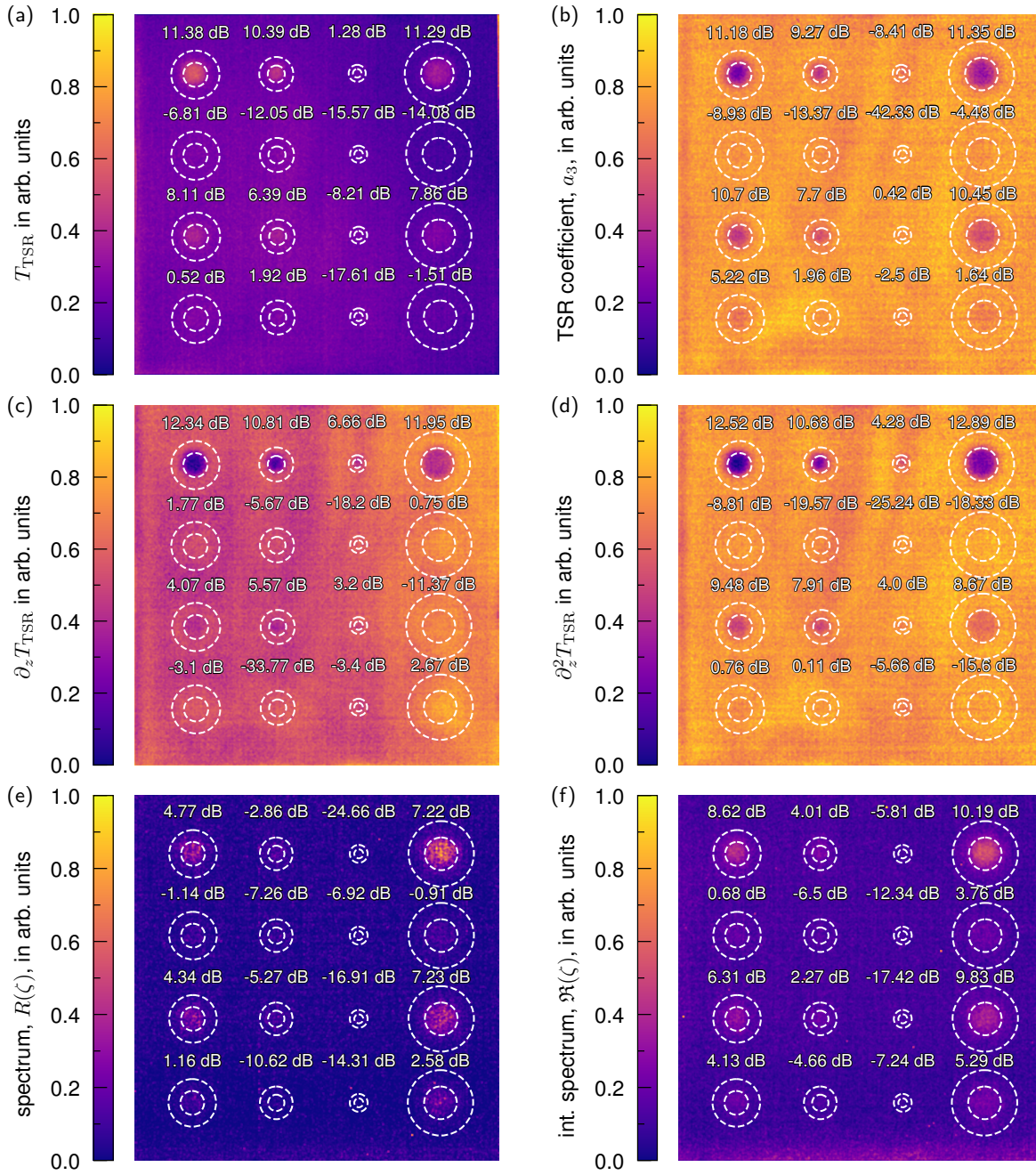
Fig. 5. *Maximum values of SNRs for pulse (flash lamp) and step excitation (halogen lamp). (a) 7th-degree TSR polynomial (T_{TSR}) using pulse excitation, (b) TSR coefficients (a_3) of the 7th-degree polynomial, (c) TSR 1st derivative (∂_z) of the 7th-degree polynomial, (d) TSR 2nd derivative (∂_z^2) of the 7th-degree polynomial, (e) time constant spectrum ($R(\zeta)$) for step excitation (halogen lamp), (f) integrated time constant spectrum ($\Re(\zeta)$) for step excitation (halogen lamp).*

evaluation methods. Nevertheless, the results achieved by each evaluation method depend on the quality of the measurement data. When comparing results of different excitation methods, this has to be kept in mind.

Comparing both excitation sources for step excitation, the defects are visible more clearly using halogen excitation. For TSR evaluation using flash excitation, the best results are provided by the 1st derivative of the polynomial. For step excitation, the best results are obtained using the integrated time constant spectrum and the halogen lamp. A total of five

Table 1. *Best SNR values in decibel (dB) for each of the 16 holes, excitation source, and method as well as their average. The holes are labelled according to the notation diameter/depth, both values in mm (Figure 1). Methods: measured temperature transient (ΔT), TSR coefficients (a_i), TSR polynomial (T_{TSR}), their derivatives (∂_z and ∂_z^2), corresponding logarithms and exponentials (exp and ln), time constant spectrum ($R(\zeta)$), and integrated time constant spectrum ($\mathfrak{R}(\zeta)$). The colour coding is a guide to the eye.*

pulse excitation (flash lamp)

	16/2	16/3	16/4	16/5	12/2	12/3	12/4	12/5	8/2	8/3	8/4	8/5	4/2	4/3	4/4	4/5	avrg.
ΔT	9.0	6.8	1.9	-1.9	9.8	6.6	1.5	-0.9	8.1	3.5	0.1	-6.0	0.0	-4.7	-5.2	-5.2	1.5
$\ln(\Delta T)$	9.1	6.9	2.1	-1.3	9.8	6.6	1.6	-0.8	8.2	3.5	-0.0	-6.1	0.2	-4.3	-4.8	-5.8	1.5
TSR, a_i	11.5	9.8	3.8	-0.4	12.3	9.0	4.3	0.7	10.4	6.6	0.4	-2.2	1.0	0.3	-2.5	-0.9	4.0
T_{TSR}	11.6	9.7	5.8	-0.1	11.8	9.1	4.8	1.6	10.6	7.2	3.9	-5.1	2.6	-3.7	-4.4	-7.6	3.6
$\exp(T_{\mathrm{TSR}})$	11.3	9.6	5.9	-0.1	11.5	9.0	4.8	1.5	10.5	7.1	3.8	-2.0	2.4	-3.7	-4.1	-8.0	3.7
$\partial_z T_{\mathrm{TSR}}$	12.0	11.2	8.8	7.5	12.3	10.1	9.5	8.2	10.8	8.4	5.2	4.9	6.9	3.5	-0.6	-6.9	7.0
$\partial_z^2 T_{\mathrm{TSR}}$	12.9	10.1	7.2	5.2	12.5	10.0	7.2	6.8	10.7	8.7	2.5	2.1	5.9	4.0	-1.0	-7.5	6.1

step excitation (halogen lamp)

	16/2	16/3	16/4	16/5	12/2	12/3	12/4	12/5	8/2	8/3	8/4	8/5	4/2	4/3	4/4	4/5	avrg.
ΔT	5.7	3.2	-1.2	-2.2	3.0	-0.1	-2.2	-6.6	-2.7	-4.3	-7.1	-8.4	-4.5	-4.8	-4.5	-2.4	-2.5
$\ln(\Delta T)$	5.6	3.1	-1.3	-2.2	3.0	-0.0	-2.3	-6.5	-2.6	-4.2	-6.5	-8.2	-4.4	-4.5	-4.7	-2.8	-2.4
TSR, a_i	-7.7	-10.7	-4.6	-9.4	-11.2	-9.9	-11.8	-14.7	-10.7	-5.5	-12.8	-14.8	-15.3	-9.4	-4.9	-3.6	-9.8
T_{TSR}	8.2	6.7	2.8	1.5	6.2	3.1	1.8	-3.7	0.8	-0.8	-8.6	-9.5	-8.6	-7.0	-5.1	-2.6	-0.9
$\exp(T_{\mathrm{TSR}})$	8.1	6.7	2.9	1.4	6.1	3.2	1.6	-3.5	0.7	-0.9	-9.2	-9.4	-8.6	-7.0	-5.2	-2.6	-1.0
$\partial_z T_{\mathrm{TSR}}$	8.5	7.9	3.9	1.1	6.6	5.2	1.6	-3.2	2.4	0.6	-4.2	-7.3	-2.7	-5.6	-2.4	-4.6	0.5
$\partial_z^2 T_{\mathrm{TSR}}$	6.2	4.8	1.6	-0.3	4.5	1.5	-1.3	-7.2	0.7	-2.3	-5.5	-9.9	-7.0	-6.2	-2.5	-10.4	-2.1
$R(\zeta)$	7.1	7.1	3.1	1.2	5.7	4.4	1.6	-1.1	0.4	-1.9	-3.8	-5.1	-3.2	-4.5	-7.6	-2.7	0.0
$\mathfrak{R}(\zeta)$	10.2	10.1	6.4	3.8	8.6	6.8	4.9	1.5	5.2	2.6	-2.6	-3.8	-4.2	-9.5	-7.1	-7.0	1.6

step excitation (LED lamp)

	16/2	16/3	16/4	16/5	12/2	12/3	12/4	12/5	8/2	8/3	8/4	8/5	4/2	4/3	4/4	4/5	avrg.
ΔT	5.0	1.8	-3.6	-3.5	2.2	-1.7	-4.8	-6.5	-1.8	-4.9	-7.0	-6.6	-2.9	-4.7	-5.5	-4.9	-3.1
$\ln(\Delta T)$	5.0	1.7	-3.6	-3.5	2.2	-1.6	-4.7	-6.4	-1.7	-4.9	-7.1	-6.4	-3.0	-4.3	-4.6	-5.0	-3.0
TSR, a_i	-5.9	-5.0	-3.2	-13.7	-9.7	-8.7	-11.9	-19.7	-6.0	-8.7	-6.8	-11.8	-6.0	-6.2	-2.5	-14.0	-8.7
T_{TSR}	8.2	5.9	-0.1	-2.1	6.5	1.1	-1.4	-6.9	1.8	-6.6	-6.5	-7.5	-5.3	-7.0	-6.5	-10.5	-2.3
$\exp(T_{\mathrm{TSR}})$	8.0	5.8	0.0	-2.2	6.5	1.1	-1.4	-7.3	1.6	-6.8	-6.4	-7.5	-5.2	-7.1	-6.6	-14.1	-2.6
$\partial_z T_{\mathrm{TSR}}$	7.7	6.7	4.4	0.9	5.6	3.9	2.8	-4.0	2.9	-0.1	-4.2	-6.1	-5.7	-3.9	-2.8	-6.8	0.1
$\partial_z^2 T_{\mathrm{TSR}}$	5.6	3.9	1.6	-3.5	3.0	-1.1	-1.9	-8.3	0.1	-5.1	-8.2	-9.8	-4.7	-2.8	-2.6	-14.1	-3.0
$R(\zeta)$	4.8	1.8	-2.3	-4.1	-2.3	-4.3	-7.7	-6.4	-7.9	-7.4	-11.6	-9.8	-4.0	-4.6	-7.9	-4.2	-4.9
$\mathfrak{R}(\zeta)$	7.9	4.9	1.7	0.4	2.9	-1.3	-3.7	-5.8	-7.2	-10.0	-10.0	-11.2	-2.0	-3.2	-8.4	-5.0	-3.1

defects are clearly identified and ten defects achieve signals above 0 dB. In all cases, using the integrated time constant spectrum, $\mathfrak{R}(\zeta)$, is superior to $R(\zeta)$. The best result is achieved by the 1st derivative of the TSR polynomial with flash excitation, recognizing 11 defects with 14 defects above 0 dB.

6. Conclusion

In this work, thermographic network identification (TNI) and thermographic signal reconstruction (TSR) are used to detect defects in a flat bottom holes reference sample. With the experimental setup used, TSR with pulse-heated excitation yields the best results. As expected, it performs better than TSR with step excitation [7]. However, it has to be kept in mind that for pulse excitation, the measured thermal transients show the defects more clearly than for step excitation. This introduces a bias when comparing methods with different excitation types.

Despite its better turn-off behaviour, LED excitation performs worse than halogen excitation. One possible reason is the lower excitation power, which is reflected in the lower total temperature difference. To overcome this issue, multiple excitation sources will be used in future measurements. In addition, a temperature-controlled heat sink can be added on the back of the sample to increase the heat flux though the sample. A higher spatial resolution of the infrared system has the potential to increase the sensitivity towards the smallest defects. Due to the spectral overlap of the flash lamp with the infrared camera, a TNI evaluation using flash excitation could not be realized.

For the case of step excitation with a halogen lamp, the integrated time constant spectrum, $\Re(\zeta)$, achieves better results than all TSR variants. The high number of detected defects shows the potential of TNI, in particular when applied to thermographic measurements with step excitation.

References

[1] V. Vavilov and D. Burleigh. *Infrared Thermography and Thermal Nondestructive Testing*. Springer Cham, 1st edition, 2020.

[2] B. Milovanović, M. Gaši, and S. Gumbarević. Principal component thermography for defect detection in concrete. *Sensors*, 20(14), 2020.

[3] E. D'Accardi, F. Palano, R. Tamborrino, D. Palumbo, A. Tatì, R. Terzi, and U. Galietti. Pulsed phase thermography approach for the characterization of delaminations in cfrp and comparison to phased array ultrasonic testing. *Journal of Nondestructive Evaluation*, 38, 2019.

[4] D. L. Balageas and J.-M. Roche. Common tools for quantitative time-resolved pulse and step-heating thermography – part i: theoretical basis. *Quantitative InfraRed Thermography Journal*, 11(1):43–56, 2014.

[5] N. J. Ziegeler, P. W. Nolte, and S. Schweizer. Thermographic network identification for transient thermal heat path analysis. *Quantitative InfraRed Thermography Journal*, 0(0):1–13, 2022.

[6] S. M. Shepard, J. R. Lhota, B. A. Rubadeux, D. Wang, and T. Ahmed. Reconstruction and enhancement of active thermographic image sequences. *Optical Engineering*, 42(5):1337 − 1342, 2003.

[7] J.-M. Roche and D. L. Balageas. Common tools for quantitative pulse and step-heating thermography – part ii: experimental investigation. *Quantitative InfraRed Thermography Journal*, 12(1):1–23, 2015.

[8] D. L. Balageas, J.-M. Roche, F.-H. Leroy, W.-M. Liu, and A. M. Gorbach. The thermographic signal reconstruction method: A powerful tool for the enhancement of transient thermographic images. *Biocybernetics and biomedical engineering*, 35(1):1–9, 2015.

[9] T.J. Kennett, W.V. Prestwich, and A. Robertson. Bayesian deconvolution i: Convergent properties. *Nuclear Instruments and Methods*, 151(1):285–292, 1978.

[10] Y. Chung, R. Shrestha, S. Lee, and W. Kim. Thermographic inspection of internal defects in steel structures: Analysis of signal processing techniques in pulsed thermography. *Sensors*, 20(21), 2020.

[11] P. Dahlberg, N. J. Ziegeler, P. W. Nolte, and S. Schweizer. Design and construction of an led-based excitation source for lock-in thermography. *Applied Sciences*, 12(6), 2022.

[12] P. Albendea, F. J. Madruga, A. Cobo, and J. M. López-Higuera. Signal to noise ratio (snr) comparison for pulsed thermographic data processing methods applied to welding defect detection. 01 2010.

[13] E. D'Accardi, D. Palumbo, R. Tamborrino, P. Cavallo, and U. Galietti. Pulsed thermography: evaluation and quantitative analysis of defects through different post-processing algorithms. In *14th Quantitative InfraRed Thermography Conference, Berlin*, 2018.

[14] A. Das and W. S. Geisler. A method to integrate and classify normal distributions, 2020.

[15] F. E. Harrell Jr. *Regression Modeling Strategies*. Springer, Cham, 2nd edition, 2015.